Scientific and Technical Information

Edition CDR 5, pp. 35–51, 12/2001

Bragg-microscopic experiments on solidifying colloidal melts

by M. R. Maaroufi, A. Stipp, Th. Preis and Th. Palberg

Institut für Physik, Johannes Gutenberg-Universität, Mainz

Leica
MICROSYSTEMS

Bragg-microscopic experiments on solidifying colloidal melts

by M. R. Maaroufi, A. Stipp, Th. Preis and Th. Palberg

Institut für Physik, Johannes Gutenberg-Universität, Mainz

Abstract:
Due to the colloid specific length scales the size, form and distribution of colloidal crystals can conveniently be studied using a combination of light scattering and microscopy. Further nucleation, growth and ripening in systems of colloidal shear melts are accessible by performing time resolved experiments. The contrast mechanism is given by the difference in $S_i(q)$ the static structure factor of different phases i under a given observation direction. We report several experimental realisations and give representative examples with a particular focus on the crystallisation kinetics. Two applications are discussed in some detail. First we observe the quasi-homoepitactic growth kinetics of oriented, monolithic but highly twinned body centred cubic crystals to obey a Wilson-Frenkel growth law above the melting line. Below, i.e. in coexistence, we observe a different growth mechanism giving rise to non-linear advancement of the crystal-melt interface as a function of time. Secondly, we investigate the coarsening behaviour of the mentioned twin domains and observe kinetics compatible with Lifschitz-Allen-Cahn behaviour. Lateral coarsening, however, ceases above a critical crystal height, and a columnar morphology results. Further applications and the limitations of the method are discussed.

Introduction

In recent years colloidal model suspensions of spherically symmetric and experimentally variable interaction have acquired a well reputated state as mesoscopic analogues of atomic condensed matter. Fundamental problems of the equilibrium phase behaviour of single component systems [1, 2] or mixtures [3], of diffusion in fluid, crystalline and glassy states [4], or of colloidal solid elasticity [5] have been addressed comprehensively. Current focus has shifted to non-equilibrium phenomena and phase transition kinetics. Here, in particular, hard sphere suspensions of sterically stabilised PMMA spheres and charged Polystyrene or Silica suspensions were investigated [6]. In all cases the specific length and time scales are on the order of the wavelength of visible light and confined to the narrow range of milliseconds to hours, such systems are readily accessible by optical methods like light scattering and microscopy [7]. Most crystallisation kinetic investigations so far have been performed by time resolved

static light scattering in Debye-Scherrer-like set-ups [8, 9] or using small angle scattering [10]. Few experiments were reported studying crystallisation via direct particle observation using microscopy [11]. The first kind of experiments is well suited to average over processes occurring simultaneously over the entire sample volume like homogeneous nucleation, depletion zone formation, growth and ripening of polycrystalline material. The second is optimised for studies of mechanistic details like heterogeneous nucleation at cell walls, defect and stacking fault formation or orientation by applied shear.

Valuable information, however, can also be gained also from observations on an intermediate length scale. Here in particular the morphology of crystals and their spatial extension as a function of time may be directly observed by polarisation microscopy or Bragg-microscopy [12, 13, 14, 15]. In combination with spectroscopy also the crystal structures may be inferred [13, 16].

The contrast mechanism of Bragg-microscopy is the structure dependent difference in intensity of light scattered into the observation direction. By suitably choosing this direction with respect to the directions of Bragg-scattering, contrast may be flexibly adjusted and even inverted. While the detection principle is similar in all set-ups reported, it is this flexibility in the choice of geometry which allows the detection of size, form and spatial distribution of crystallites growing within a melt, of lateral twinning occurring in epitaxially grown wall crystals or of concentric distributions of several different phases in the partial solidification of shear melts. Since colloidal time scales are conveniently large, time resolved measurements may yield nucleation rates as well as growth and ripening velocities. Most studies reviewed use a rectangular flat cell. This is the ideal geometric situation to observe the propagation of a planar crystal-melt interface of defined crystallographic direction, and also for studies of the twinning morphology. If connected to an closed circuit preparation system, systematic measurements of the growth velocity in dependence of the interaction parameters salt concentration, particle density and charge may be performed and analysed.

The aim of this paper therefore is twofold. First, we review the possibilities of Bragg-microscopy in different realisations as used by us and other authors. In this section emphasis is on technical aspects. Second, we will address two specific open questions concerning the solidification kinetics of repulsive spheres. Here the focus is on deviations from reaction controlled growth usually observed for samples completely solid at equilibrium and further on the kinetics of twin domain ripening.

Bragg microscopy

Bragg microscopy exploits the differences in scattered intensity from different sample regions, e.g. between differently oriented crystallites or between melt and crystal phase. To illustrate this, it is instructive to first recall some basics of static light scattering. Most of the concepts used have been developed in X-ray scattering and were adapted to light scattering. Here and there the magnitude of the scattering vector **q** is given by:

$$|\mathbf{q}| = |\mathbf{k_i} - \mathbf{k_S}| = (4\pi\, \nu_S/\lambda_0)\, \sin(\Theta/2), \quad (1)$$

where $\mathbf{k_i}$ and $\mathbf{k_S}$ are the wave vectors of incident and scattered light, respectively, ν_S is the refractive index of the solvent, λ_0 the vacuum wave length of incident light and Θ the scattering angle. For monodisperse spherical particles the scattered intensity factorises according to [17]:

$$I(\mathbf{q}) = C\, P(q)\, S(\mathbf{q}) \quad (2)$$

where the constant C:

$$C = \frac{V_S I_0}{R_D^2} \frac{\mathbf{k}_i^4}{(4\pi)^2} \frac{N}{V_S} (\mathbf{n_i} \cdot \mathbf{n_S})^2 b(0)^2 \quad (3)$$

comprises the geometry of the scattering experiment and the optical properties of the particle material. Here $I_0 = {}^1\!/_2\, (\varepsilon_s/\mu_0)^{1/2} E_0^2$ is the incident intensity, R_D is the distance between scattering volume V_S and the detector, $\mathbf{n_i}$ and $\mathbf{n_S}$ are the polarization vectors of incident and scattered light, respectively. The particle scattering amplitude at zero wave vector is given by the difference in refractive indices of particles and solvent times the particle volume: $b(0) = (\nu_P - \nu_S)\, (4/3)\pi a^3$. The particle form factor $P(\mathbf{q}) = b(\mathbf{q})^2/b(0)^2$ is normalized by $b(0)^2$ to result in $P(0) = 1$. It describes the angle dependence of single particle scattering. To be specific, for small Polystyrene spheres ($\nu_P = 1.590$) of $a < 60$ nm in water ($\nu_S = 1.333$) it often is sufficient to use the Rayleigh-Debye-Gans approximation for small q data:

$$b(q) = \frac{4p(\nu_P - \nu_S)}{q^3} (\cos(qa) - qa \sin(qa)) \quad (4)$$

Polydispersity, bimodal mixtures, deviations from spherical shape and the corresponding influence of particle orientation may also be treated within extensions of this approximation [18]. For larger particles and those with radial variations in ν_P Mie scattering theory applies.
$S(\mathbf{q})$ contains all the information about the particle positions $\mathbf{r}_i$. It is defined as:

$$S(\mathbf{q}) \equiv \frac{1}{N} \sum_{i=1}^{N} \sum_{j=1}^{N} \left\langle \exp(i\,\mathbf{q} \cdot (\mathbf{r}_i - \mathbf{r}_j)) \right\rangle \quad (5)$$

where the brackets <...> denote the ensemble average. $S(\mathbf{q})$ differs for differently structured phases.

So far both Debye-Scherrer powder scattering patterns and two dimensional scattering patterns of oriented single crystals were reported. In the first case the sample typically is placed in a vertically mounted cylindrical cell and illuminated by a broadened laser beam. The scattered intensity is recorded under different angles in the plane normal to the cell axis to yield a Debye-Scherrer Powder pattern exhibiting characteristic peaks [19] . An example is given in Fig. 1a with the corresponding Miller indices identifying the structure to be body centred cubic. Fig. 1b compares the scatter-

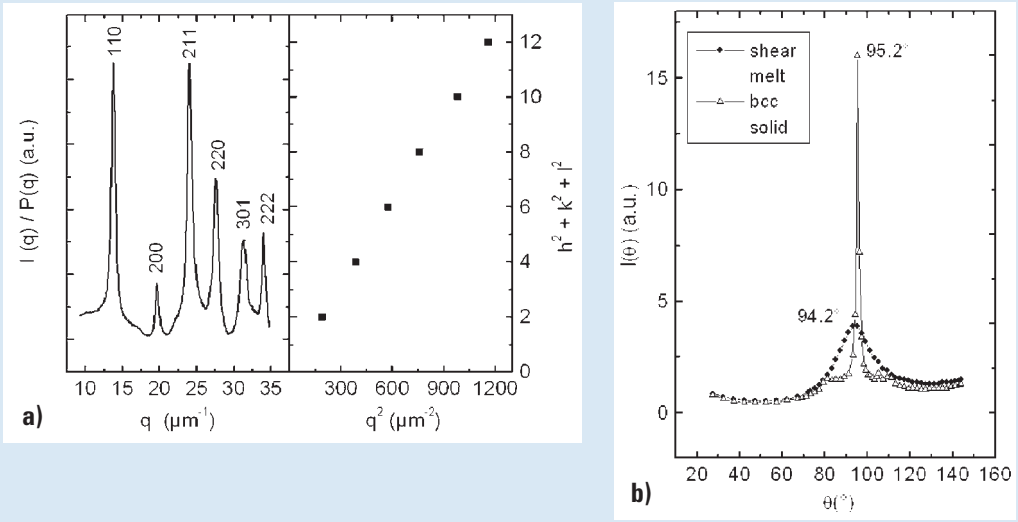

Fig. 1: Debye Scherrer powder patterns of a deionised aqueous suspension of Polystyrene latex particles. **a)** fully crystalline bcc structure; **b)** comparison of patterns obtained for the solid and the shear melt at the same particle number density.

ing pattern of a crystal powder to that of the corresponding shear melt in the vicinity of the first peak in the structure factor.

The scattering contrast is clearly visible in particular in the vicinity of the main peak. Throughout solidification crystallites coexist with remaining fluid. If particle positions in different phases are uncorrelated, in reciprocal space a superposition of melt and crystal scattering is observable. In Bragg microscopy therefore the detector is replaced by a microscope or camera with macro lens positioned under a suitably chosen observation angle. Depending on this angle and illuminating wave length bright, Bragg scattering crystals are visible in a background of less scattering fluid or non-scattering other crystals. For sufficiently large crystals their shape and size may be recorded with great accuracy. Use of white light illumination increases the number of Bragg reflecting crystals. A typical example of the resulting colourful mosaic of crystallites (much like in natural gem opal) is shown in Fig. 2 for a sample of micro-network spheres. We note that while an additional colour contrast is achieved, the intensity contrast is somewhat diminished under white light illumination. Like in polarisation microscopy limitations are encountered in thick samples, where the contrast vanishes due to superposition of light stemming from regions off the focal plane [12, 20, 21].

This particular realisation of Bragg-microscopy has been used in several studies on crystal morphologies by Okubo [13, and references therein] and in the pioneering growth velocity studies of Aastuen et al. [14]. In particular at low nucleation rates resulting in few large crystals there still are statistical limitations, as only in rare cases a Bragg-reflection will hit the camera. An improved version was recently reported, now using a slit illumination and placing the camera somewhat off the Bragg-angle. Then crystalline regions can be distiguished by their diminished scattering power as compared to the surrounding melt independent of their respective orientation [22]. They have been termed “ghost crystals”. This contrast inverted Bragg-microscopy shows a significantly improved statistical accuracy.

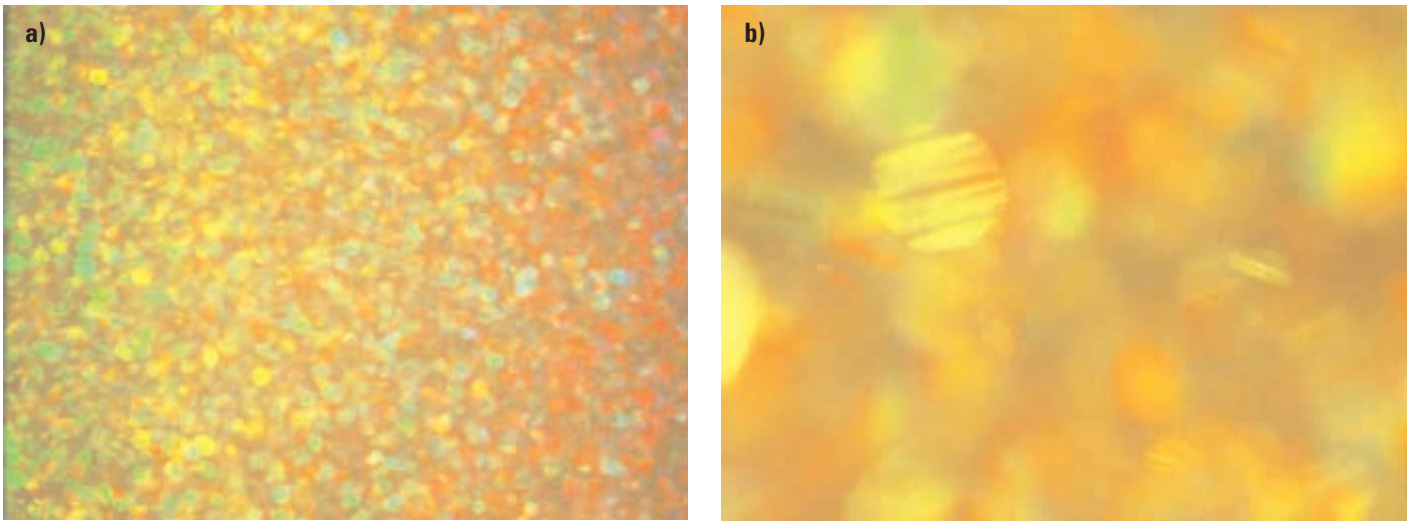

Fig. 2: Bragg-micrographs of crystalline micro-network sphere suspensions at **a)** high and **b)** moderate packing fraction. The image size corresponds to 2.3 x 3.2 mm^2. Note the increase in crystallite size and the corresponding decrease in crystallite density. Note further the stripe pattern of the crystals in **b)** which originates from a twinned fcc structure.

An alternative approach is the growth of oriented single crystals from shear melts produced in parallel plate thin cells. In such geometries heterogeneous nucleation at the cell wall with subsequent homoepitaxial growth prevails under most sample conditions [11]. It is further favoured by the fact that in most cases shear is applied to produce the melt phase in the first place. If the shear is directed, large monolithic but twinned crystals are obtained showing a well defined orientation of the principal crystallographic directions throughout the whole sample. Depending on the crystal structure twins appear either as neighbouring columnar structures (bcc) or as stacking faults in fcc crystals [23] (cf. Fig. 2b).

In Fig. 3a–c we give examples of two-dimensional scattering patterns as observed on a screen behind a sample contained in a thin rectangular cross section flow-through cell and illuminated by a laser beam. Scattering patterns were recorded across the body centred cubic (bcc) – face centred cubic (fcc) phase transition. All were taken after complete solidification. Both single phase scattering pattern are superpositions from twin

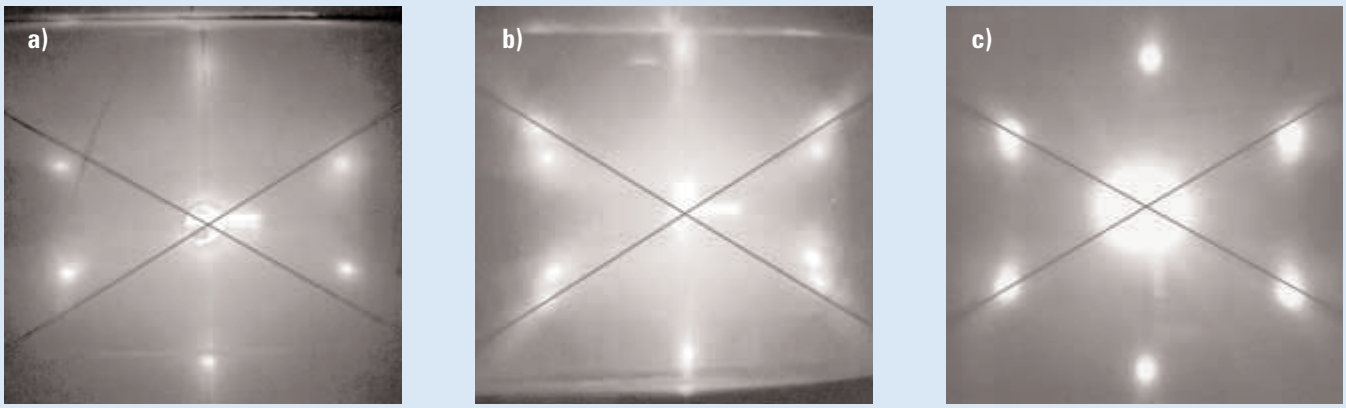

Fig. 3: Two dimensional scattering patterns of oriented crystals of deionised charged latex spheres (PS120, see below). **a)** twinned bcc pattern at low n, **b)** superposition of bcc and fcc patterns in the coexistence region 2.8 $\mu m^{-3} < n < 4.3\ \mu m^{-3}$; **c)** twinned fcc pattern at large n.

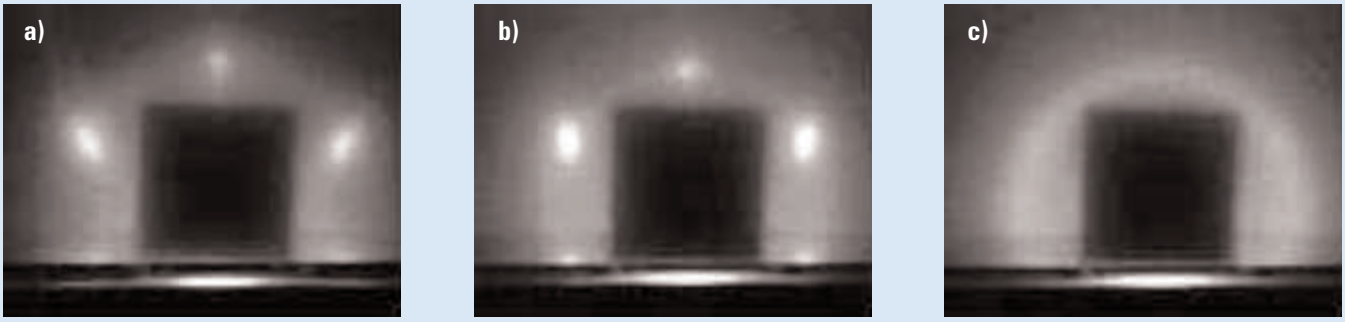

Fig. 4: Two dimensional scattering patterns of deionised PS120 as observed in a flow through cell of rectangular cross section **a)** fcc pattern at mechanical equilibrium; **b)** at moderate shear fluxes we observe the superposition of a hexagonal scattering pattern emerging from randomly stacked triangular planes and a ring pattern produced by the isotropic shear melt; **c)** at large fluxes the same superposition is observed with reversed amplitudes. As can be seen from Fig. 6A, the system is completely shear molten except for a very thin region with wall stabilised layer structure.

scattering patterns, each comprising of four (three) Bragg spots for the bcc (fcc) case [9, 24]. Under shear flow non-equilibrium phases may be stabilised. Fig. 4a, b, c gives an example taken on a rectangular flow-through cell with approximately parabolic flow profile. Here at low overall flux a crystal-like phase of oriented hexagonal layer structure is observed (Fig. 4a), while at high flux an isotropic shear melt prevails (Fig. 4c). At intermediate fluxes both structures coexist and the scattering patterns superimpose. Scattering of the layer phase is constrained to six equivalent Bragg spots, while the fluid phase generates a broad ring pattern. The coexistence of a few layers of hexagonal order next to the cell wall is only faintly visible in Fig. 4c as superimposed spots. If shear is aborted in the latter case the wall layers act as nucleus for subsequent growth against an isotropic shear melt.

Clearly, the appearance of the Bragg microscopic pictures now strongly depends on the choice of both the polar Θ and the azimuthal angle φ. For instance, Würth et al. [15] chose an illumination with a laser beam and off peak angle combination for detection resulting in a ghost crystal [15]. An example is given in Fig. 5.

A good contrast was achieved at all times. The spatial resolution was limited by blurring due to the limited dynamic range of the CCD-camera used and the macro-lens resulting in a comparably low magnification. Resolution was enhanced by a long transmission length of the laser beam crossing the cell under an angle off the surface normal. The visible length still corresponds to the cell depth of 1 mm. Line intensity analysis of the time resolved recording nevertheless allowed the determination of the growth velocity from a plot of crystal thickness versus time with great accuracy.
Determination of phase distributions is not restricted to the coexistence of two phases. To study shear flow through a cylindrical tube v.Hühnerbein et al. used an illumination perpendicular to the cell wall and choose the upper Bragg spot of Fig. 4b [25]. In this case homogeneously nucleated crystals in the tube centre only rarely contributed to the scattering pattern. Rather shear induced layer structures were visible with high and shear melt with low intensity to form a concentric phase distribution. An example of resulting flow dependent Bragg micrographs is shown in Fig. 6. Here the overall flux decreases from A to G. Note the small region of oriented

Fig. 5: Bragg-micrographs of a melt solidifying in a cell of rectangular cross section taken under an observation angle not fulfilling the Bragg condition. From top to bottom **a)** t = –20 s: under shear the system is completely shear molten. **b)** cessation of shear determines t = 0. **c)** t = 60 s: as two crystals grow inside from both cell walls the region of high intensity shrinks; **d)** t = 200 s: final completely solidified state.

Fig. 6: Bragg micrographs of the stationary phase distribution in a aqueous suspension of charged latex spheres (particle radius 52 nm, particle number density n = 4.5 1018 m^{-3}, thoroughly deionised) flowing through a cylindrical tube taken at an observation angle fulfilling the Bragg condition for the layer phase. The overall flux decreases from A to G. The polycrystalline core expands on expense of the shear melt and the layer phase. The latter is located both at the cell wall and on the core region.

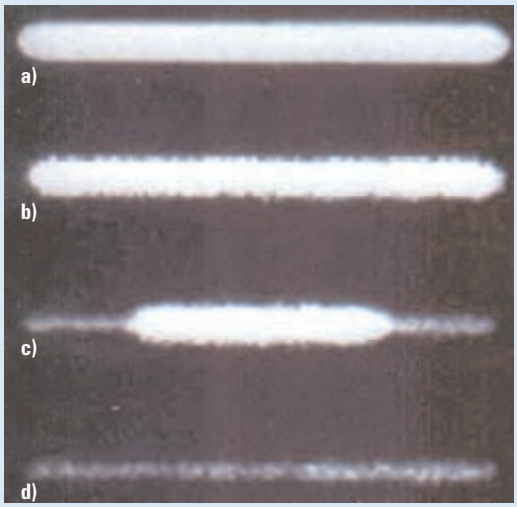

Fig. 5

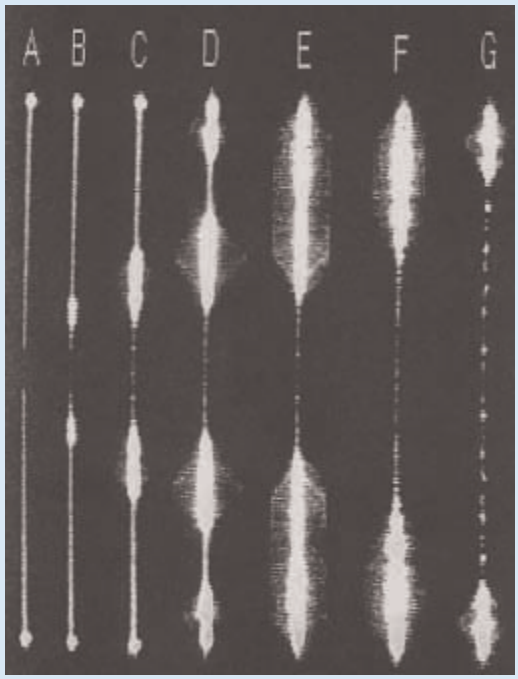

Fig. 6

layer phase present at the cell wall even at highest fluxes. It may serve as nucleus after abortion of shear.

Both realisations of Bragg microscopy mentioned above used a laser illumination and a detecting camera deliberately positioned with respect to the resulting scattering pattern. For the experiments reported below we intended to image broader parts of the sample and with higher resolution. To this end we mounted a rectangular cell on the stage of an optical microscope Leitz Laborlux 12 Pol S (Leica Wetzlar) with an objective of 5-fold magnification. Illumination was performed with a flexibly adjustable cold white light source. We thus inverted the scattering geometry as compared to the situation of Fig. 3. Instead of illuminating a sample with parallel light incident perpendicular to the cell wall, the direction of the incoming beam is chosen such, that the scattered light of one phase or morphology of interest is emitted perpendicular to the cell wall and can be collected by a microscope objective. Fig. 7 compares both geometries. In both schematic drawings light enters the cell from below. The different crystal phases are drawn hatched in different directions. If in the scattering set-up different Bragg reflections are observed to emanate from different structures or orientations, one of these is chosen for the illumination angle combination. We note that in a rectangular cell four wall crystals are growing: two vertically from the top and bottom and two horizontally from the cell sides. For sufficient cell depth both can be monitored independently. Images a and b of Fig. 8 were taken from a cell of depth d = 5 mm filled with a completely deionised suspension of PS120 (for sample details see below) at n = 2.8 $\times$ 10^{18} m^{-3}. The observation region is 3.2 $\times$ 2.4 mm^2 as calibrated from an optical standard. In Fig. 3 c and d the cell was observed further away from the side wall to picture the morphology of crystals growing from both cell bottom and top. Here illumination was performed from one of the twin specif-

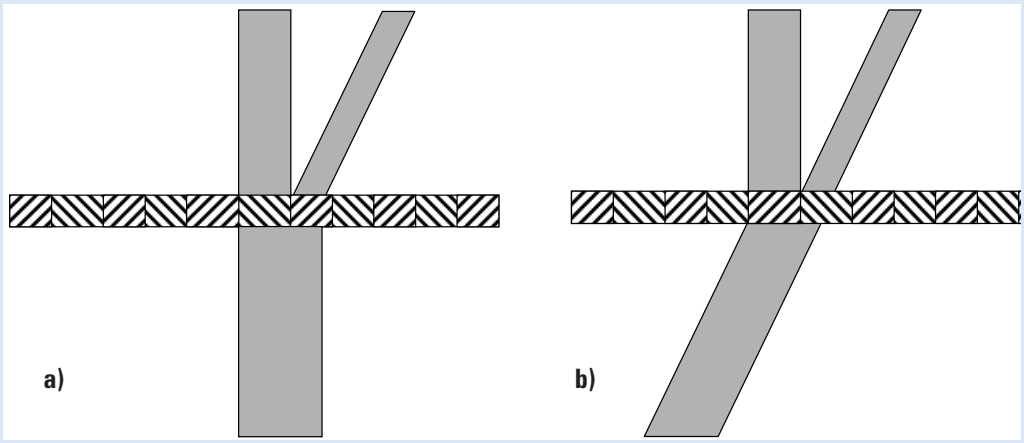

Fig. 7: Schematic drawing of **a)** Bragg scattering as used in the experiment of Fig. 3; **b)** Bragg microscopy as used in the experiment of Fig. 8. Different twin domains are hatched differently. Illumination is from below a) perpendicular to the cell surface; **b)** under Bragg condition for one of the twins.

ic directions. One observes the formation of cloud-like, longish objects from originally more isotropic lateral nuclei [26].

Further, in the early stages of this latter case scattering from the melt dominates resulting in a comparably poor contrast. The necessary crystal thickness to obtain a good contrast of say 2:1 was determined from the thickness of the side wall crystal at the instant when this contrast was reached to be on the order of some 20 lattice constants. Note from Fig. 8a and b that no twin boundaries are observed in growth direction. Only lateral twinning occurs. Thus in Fig. 8c and d two sheets of columnar twins are formed giving rise to only three different intensities.

The recorded time resolved Bragg images were further processed by image analysis yielding the crystal thickness z(t) and the average lateral dimensions x(t) and y(t). Even if a low resolution picture is taken, the crystallisation velocity can be obtained with high accuracy from a time sequence. In Fig. 8a and b the wall nucleated crystal grows away from the

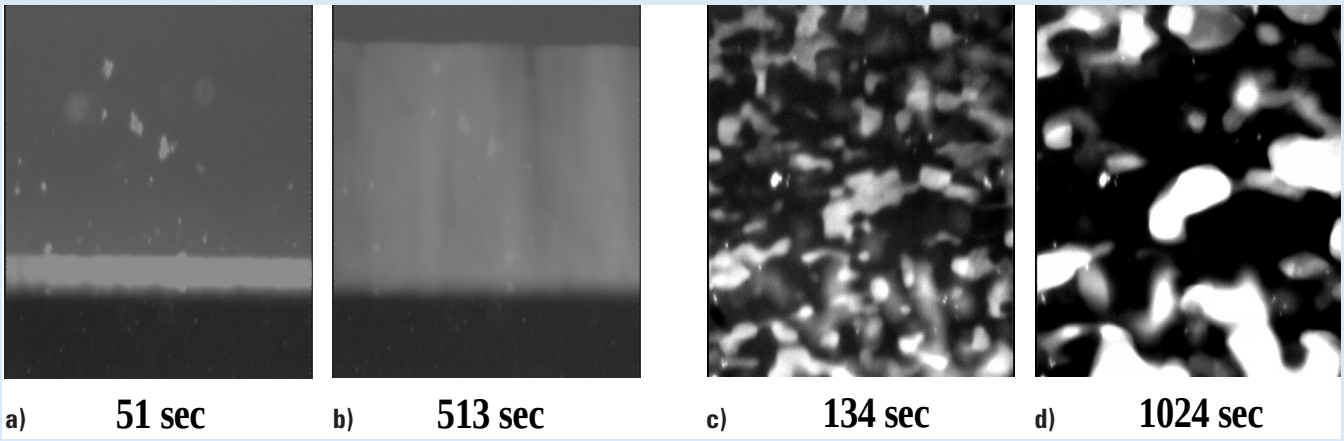

Fig 8: Bragg microscopic pictures as taken from a deionised suspension of PS120 solidifying from the shear melt. Shown area corresponds to 3.2×2.4 mm^2. Left side: growth of a wall crystal nucleated at one of the side walls of the rectangular cell. Here the top Bragg spot direction in Fig. 1c is used for illumination; right side: lateral twin domain pattern for crystals growing from the cell top and bottom as observed top on. Picture taken near the cell center. Coarsening of twin domains appears during continued growth. A columnar morphology results.

Table 1: Sample data

Sample	Manufacturer	Batch No.	Nominal diameter 2a / nm	Titrated charge Z	Conductivity charge Z^*_σ	Elasticity charge Z^*_G
PS120	IDC	10-202-66.3	120	3600	685 ± 10	485
PS156	IDC	2-179-4	156	5180	945 ± 70	607

side wall at constant speed of some 6 μm/s^{-1}. Also the lateral twin domains evolve in time, becoming more compact in shape and at the same time increasing in size. We shall now discuss these two examples in more detail and focus on the kinetic data that can be extracted from such measurements.

Kinetic experiments on solidifying charged sphere suspensions

Two species of commercially available Polystyrene latex spheres, PS120 and PS156, were investigated. The particle parameters are compiled in Tab. 1. All suspensions were prepared from diluted and pre-cleaned stock suspensions of approximately 1% packing fraction. The suspensions were further thoroughly deionised using advanced continuous conditioning methods. Details of this have recently been given elsewhere [27]. Both individual species were comprehensively characterised before conducting the solidification experiments.

Both pure samples crystallise at low particle number densities in a body centred cubic structure (bcc). Measurements of the static structure factor S(q) were further used to calibrate measurements of the conductivity σ. The particle number density dependence of σ was observed to be strictly linear and independent of the phase state of the suspension. Data for thoroughly deionised suspensions are well described by $\sigma = n\, e\, Z^*_\sigma\, (\mu_p + \mu_+) + \sigma_B$ with the elementary charge e, the particle, respectively proton mobilities μ_p and μ_+, and the background conductivity σ_B (mainly stemming from dissociated water and ionic impurities). The effectively transported charge Z^*_σ was determined as fit parameter. It is tabulated in Tab. 1. The shear modulus G is on the order of a few Pa and in good agreement with theoretical fits yielding an effective shear modulus charge of Z^*_σ as only free parameter [5]. Both samples were used for growth experiments and PS120 was further used in the twin ripening experiments.

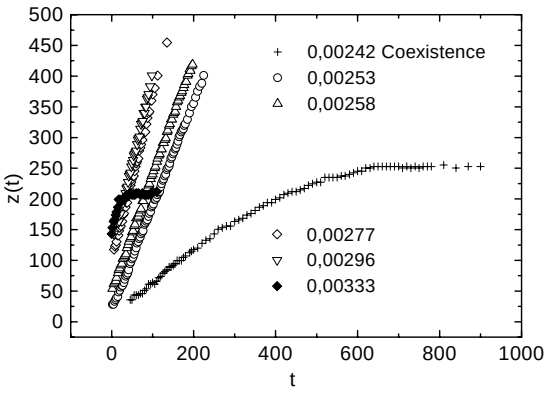

Fig. 9: Vertical extension of wall nucleated crystals as a function of time. Different symbols correspond to different packing fractions.

Homoepitactic growth of oriented monolithic crystals

This section deals with the growth velocity of wall nucleated crystals. The velocity can be directly inferred from time sequences of Bragg micrographs (c.f. Fig 8a). For illustration we plot the crystal thickness z(t) for deionised suspensions of PS156 of different packing fraction $\Phi = n\, V_P$, where n is the particle number density and V_P the particle volume in Fig. 9.

We note that compared to PS120 a rather broad coexistence region is observed, facilitating measurements also within the coexistence region. Three different scenarios are observed. Above melting growth is linear. For not too large Φ solidification proceeds exclusively via growth of wall crystals. On the other side, above $\Phi = 0.0031$ wall crystal growth is stopped by homogeneously nucleated crystals in the bulk. In both cases growth is reaction controlled, i.e. determined by the registering of particles from the melt at their target positions in the crystal. However, across coexistence growth is much slower, and more importantly non-linear in time.

This is partly due to a change in the growth scenario. Above melting the transition occurs without a net change of density and linear growth results. Across coexistence the suspension phase separates into crystal and fluid which have a considerable density difference. Thus in addition of the registering of particles at their target place a second kinetic processes is involved. Particles are transported towards the crystal-melt interface by collective diffusion. This results in a continuously slowed growth. If this process dominates, a diffusion limited $t^{1/2}$ growth is expected. In addition growth is slowed as the final state consisting of fluid plus crystal of finite thickness is approached. As the crystal grows the chemical potential difference of the remaining (diluted) melt as compared to the crystal state continuously decreases. This corresponds to a vanishing driving force for the transition and finally in a termination of growth.

In comparison, for hard spheres a transient density difference occurs also above coexistence. As collective diffusion is very slow as compared to self diffusion responsible for the registering, this results in the formation of depletion zones and a $t^{1/2}$ growth law [8, 9]. In addition, transient compression/relaxation of the crystal occurs and complex situations may arise from the overlap of depletion zones [8]. Both experiments and numerical calculations of time dependent crystal dimensions show considerable deviations from linear or $t^{1/2}$ growth and the existence of long lived transients [28, 29]. Still other scenarios are sometimes observed in micro-network colloids with near hard sphere interaction [30].

Previous studies have shown that for charged spheres above melting the growth velocity in general follows a Wilson Frenkel (WF) law [6].

$$v = v_\infty [1-\exp(-\Delta\mu/k_BT)] \qquad (6)$$

Here v_∞ is the limiting growth velocity, $\Delta\mu$ is the difference in chemical potential between melt and solid and k_BT is the thermal energy. v increases with $\Delta\mu$ and saturates for large $\Delta\mu$ at a value determined by the time scale of the elementary step of particle addition. Across coexistence data are still rare but there have been indications that the validity of WF is limited to the range above melting [6]. Here we observed non-linear growth. To extract an estimate of the initial growth velocity a linear fit at short times was performed. The resulting n-dependent growth velocities are shown in Fig. 10 and a comparison to the WF-law is given in Fig. 11.

As already discussed elsewhere, a good description of data is achieved using the thermodynamic somewhat inconsistent approximation of the chemical potential difference $\Delta\mu$ by $\Delta\mu = B\Pi^*_m$, where B is a proportion-

Fig. 10: Growth velocities for deionised PS120 versus particle number density n.

Fig. 11: Semi-logarithmic plot of growth velocities versus the reduced energy density difference between melt and melt at the phase boundary. Solid and dashed line correspond to fits of Eqn. (8) with Π^*_m (solid line) resulting in a better description of the data than the thermodynamically consistent Π^*_f (dashed line).

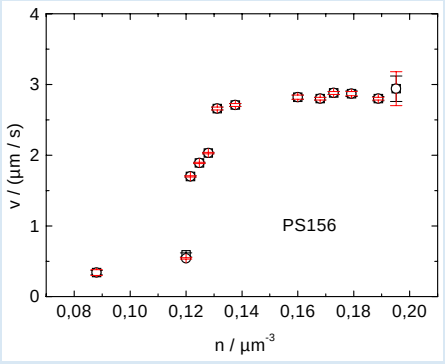

Fig. 10

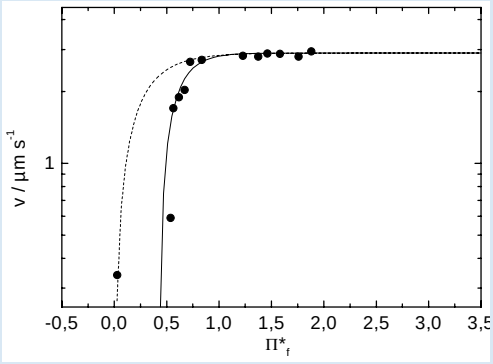

Fig. 11

ality constant of order 10 k_BT and $\Pi^*_m = (\Pi - \Pi_m) / \Pi_m$ a reduced energy density difference between the melt and the melt at melting (solid curve) [6, 15]. Here $\Pi = \alpha$ n V(d_{NN}) with the number of nearest neighbours α, the particle number density n and the pair energy of interaction at the nearest neighbour distance V(d_{NN}). Using $\Delta\mu = B\Pi^*_f$, where normalisation is performed with the thermodynamically consistent value of Π at freezing, clearly shows that across coexistence growth is about an order of magnitude slower than predicted (dashed curve).

In Fig. 12 we compare all soft sphere data currently available. Freezing is located at $\Delta_\mu = 0$. Locations of melting are indicated by arrows. As compared to previous measurements, the restriction of validity of Eqn. (8) to the region above melting is more pronounced for samples like PS156 showing a broad coexistence region.

Fig. 12: Semi-logarithmic plot of gowth velocities versus difference in chemical potential between metastable shear melt and crystal. Comparison of available charged sphere data. PS91 was studied by Aastuen et al [14] and PS 109 by Würth et al. [15]. Lines are fits of Eqn. 8 to the data. In all cases WF-growth is observed to apply above melting.

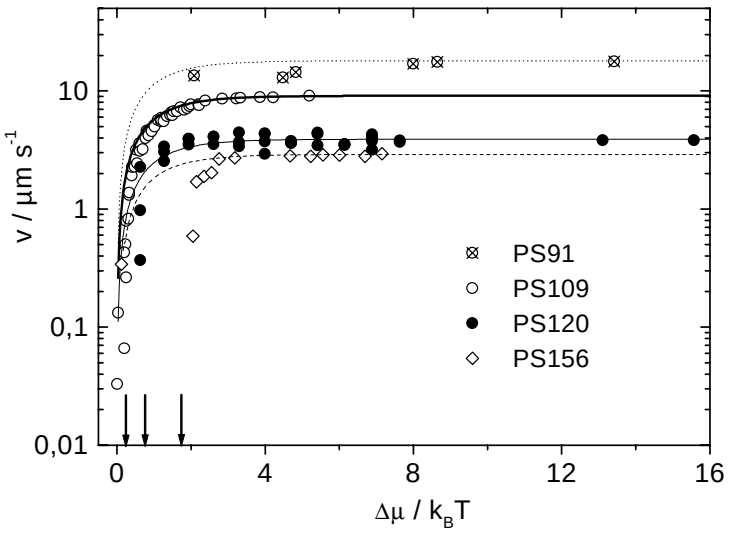

Lateral coarsening of bcc twin domains

Under shear a narrow region of oriented planes in the vicinity of the cell wall evolves (cf. Fig. 6). By mechanisms not yet known in detail this is transformed to a stacking of bcc (110) planes or fcc (111) planes, depending on the equilibrium structure of the solid (cf. Fig. 3). In both cases twinning is observed. For fcc this corresponds to the formation of stacking faults [31, 32]. For bcc columnar twin domains are formed [26]. We here investigate their lateral coarsening (cf. Fig. 8b and c). In all cases we observed small roundish to irregular domains often assorted in rows parallel to the former flow direction, the x-direction. Analysis of the scattering pattern shows that their (110) plane is parallel to the cell wall and the <111> direction is aligned parallel to the former flow. This is in agreement with previous investigations [6, 7, 9]. Average sizes in x and y direction were determined by computer aided image processing as follows. A grid is superimposed

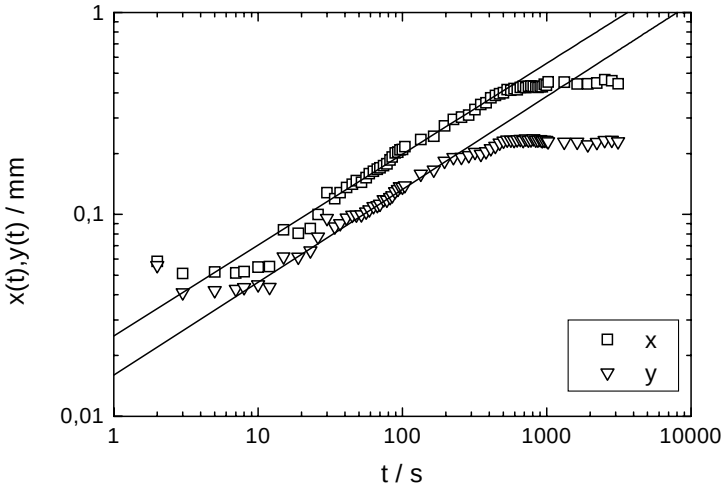

Fig. 13: Double logarithmic plot of the lateral extension x(t) and y(t) of twin domains versus time. The data are fitted by power laws with exponents on the order of 0.5 as expected for ripening with conserved order parameter. Note, however the completely unexpected termination of ripening after some hundred seconds. Note further, that gowth in z-direction still continues.

on the image, as to intersect every domain by several lines. The size of domains is measured along these lines and a weighted average performed first for each crystal, then for each image. While the use of the above described algorithm yields a small scatter of extension data in individual runs, the reproducibility between different runs at equal preparation conditions is much worse. This is attributed to a complex dependence of the domain shape on the previous shear history.

For all preparation conditions, however common qualitative features are observed. First, coarsening follows a power law behaviour indicating domain growth via displacements of grain boundaries. Second, coarsening shows a significant anisotropy. Third, in both directions the coarsening velocity is large at short times, but slows to zero for long times. And finally, the dependence of initial coarsening velocities is not incompatible with a WF-law. We shall now comment on these points in some detail.

Concerning the coarsening mechanism there are two alternative predictions for the limiting cases of the ripening behaviour of crystals. Lifshitz-Slyosow or Ostwald-ripening corresponds to ripening of a minority phase mediated via transport through a majority phase of differing order parameter. This scenario predicts a $t^{1/3}$ power law for the domain sizes. On the other hand Lifshitz-Allen-Cahn (LAC) corresponds to ripening with conserved order parameter, e.g. via grain boundary motion. Here a $t^{1/2}$ power law is predicted. In Fig. 13 we plot x and y data of one run in a double logarithmic fashion and find them to be well described by power laws $x(t),y(t) = At^a$ over more than two decades in time. No systematic dependence of a on n nor on the direction of coarsening is detected. Average values are well compatible with LAC ripening.

A striking feature of the studied twin domains is their pronounced shape anisotropy which increases with time. We suspected this to be due to an anisotropy in the ripening velocities. To quantitatively check this we performed linear fits to the data at short times as shown in Fig. 14 for the run of Fig. 13. At very early times the scatter of data is large due to insufficient contrast. An approximately linear growth is observed for 30 s < t < 100 s. In the case shown the limiting short time coarsening velocities were found to be 1.33 μms^{-1} and 0.73 μms^{-1} for x and y-direction, respectively. In general, coarsening velocities are considerably smaller than growth velocities and on average coarsening is slower by a factor of two in y-direction than in x-direction. The ripening velocity anisotropy is presumably caused by differences in the domain wall structure for both directions.

Fig. 14: Lateral extension x(t) and y(t) of twin domains versus time for short times. Data are well approximated by linear growth for 30 s < t < 100 s.

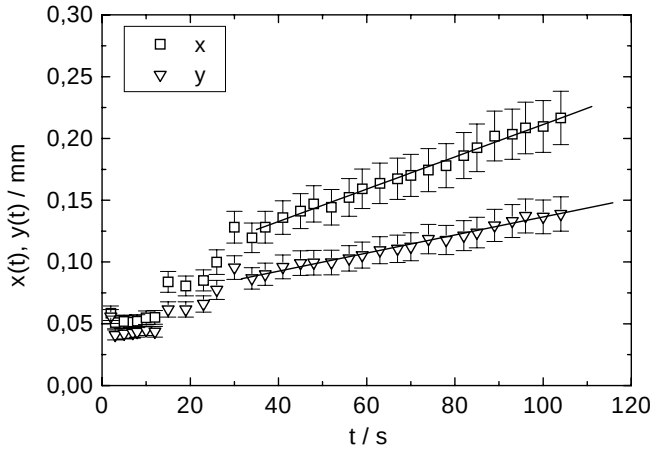

The most important result, however is the termination of ripening observed for both directions. This finding is rather surprising, as ripening is expected to slow but not to halt. In fact, bulk coarsening in hard sphere suspensions was observed to continue over the whole experimental time scale of days [8, 9, 10]. Also for a strongly twinned fcc monolithic crystal, the annealing of stacking faults was reported to continue for very large times and the data could be described by an exponential slowing [31].

At present we are unaware of a simple explanation of the observed termination of twin domain ripening. A possible explanation could be given by the assumption of collective rearrangements of particles extending over the complete crystal thickness z(t). Such a collective shift of lattice planes could imply an intermediate state of higher surface energy depending on the details of the in-plane structure. As z(t) increases linearly in time, also the lattice plane area and thus the activation energy would increase. In turn the growth velocity would exponentially decrease. This decrease is superimposed on the normal decrease caused by LAC ripening. As yet the data quality is not sufficient to fit the correct expression for the time dependence. Following Dux et al. we therefore approximate x(t) and y(t) by:

$$x(t) = x_\infty \left(1 - \exp\left(\frac{t}{\tau_x}\right)\right); \quad y(t) = y_\infty \left(1 - \exp\left(\frac{t}{\tau_y}\right)\right) \tag{7}$$

where x_∞ and y_∞ are the saturation extensions. Fig. 15 shows the data of Fig. 13 in a linear fashion with corresponding fits of Eqn. (7). The data are described fairly well supporting our hypothesis.
Further support may be taken from the differences in termination times τ. A detailed analysis shows that τ_x and τ_y are slightly different and depend on the particle number density. From these $z(\tau_{x,y})$ the thickness of the crystal at this instant may be inferred in terms of the number of (110) planes, if the growth velocity v (in z direction) and the lattice constant are known. Fig. 16 shows this height to decrease with increasing n. Approximating the activation energy density as $\Delta\Pi = (\alpha^* - \alpha)\, n\, V(d_{NN})$ where α^* is the number of nearest neighbours in the activated state, the actual activation energies

Fig. 15: Lateral extension x(t) and y(t) of twin domains versus time. The general form of the experimental curves is well described by fits of Eqn. (7).

Fig. 16: Crystal thickness given in numbers of (110) planes at the instant of termination of ripening in x and y-direction versus particle number density.

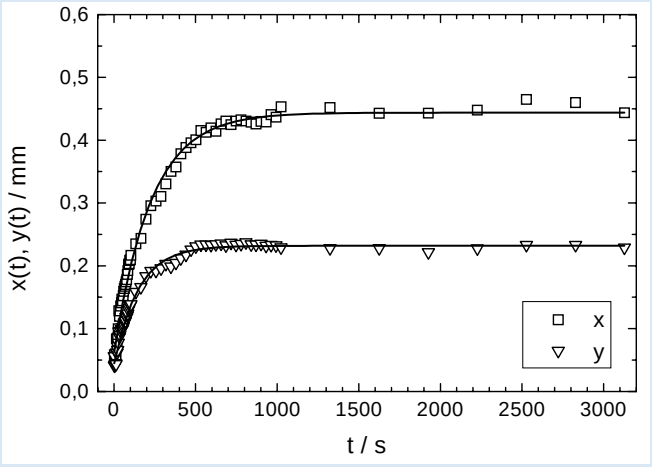

Fig. 15

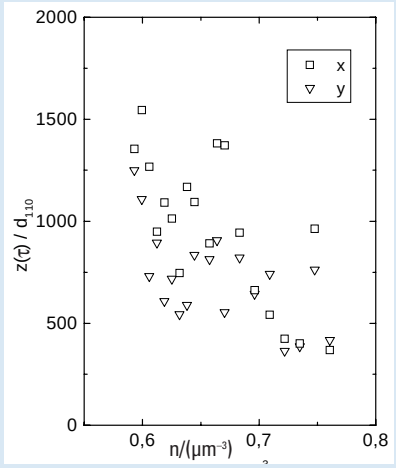

Fig. 16

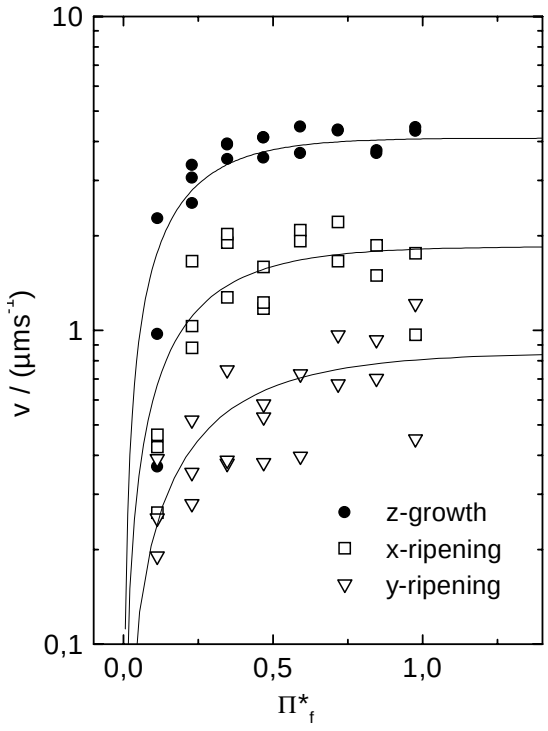

Fig. 17: Growth and initial ripening velocities versus the reduced energy density difference between melt and melt at freezing compared to different functional forms of their dependence. Solid lines are fits of Eqn. (8) using $\Delta_\mu = B\,\Pi^*_f$.

are $\Delta E_x \propto d_{NN}\, y(t)\, z(t)\, (\alpha^*_x - \alpha)\, n\, V(d_{NN})$ and $\Delta Ey \propto d_{NN}\, x(t)\, z(t)\, (\alpha^*_y - \alpha)\, n\, V(d_{NN})$, respectively. Thus with larger n a smaller $z(\tau)$ is needed to increase ΔE beyond the thermal energy. If $y(\tau)$ was constant a direct proportionality would result. Here z(t) decreases by a factor of two while n is increased by some 20%. For different interfacial structures, i.e. for different α^*, different $z(\tau)$ should result as indeed was observed: coarsening x-direction terminates later.

We finally check for a Wilson-Frenkel like behaviour of ripening. The functional dependence may possibly be expected considering Thompson's rule stating that the excess energy of a particle in a grain boundary as compared to the crystal is approximately half the value of a particle of the melt [33]. Then the surface tension driving ripening would be proportional to Π^*_f, too, albeit with smaller B. In Fig. 17 we plot the observed initial velocities versus Π^*_f. We note an unusually large scatter of data for this specific sample. It was presumably due to a leak in the sample cell unnoticed during the experiment. In addition, due to the image analysis procedures applied the scatter is considerably larger for coarsening than for growth. We obtained the following values for the fit parameters: $B_z = 4.6 \pm 0.9\ k_BT$ and $v_{\infty,z} = (4.3 \pm 0.3)\ \mu ms^{-1}$; $B_x = (4.6 \pm 1.5)\ k_BT$ and $v_{\infty,x} = (1.8 \pm 0.2)\ \mu ms^{-1}$; and $B_y = (2 \pm 1)\ k_BT$ and $v_{\infty,y} = (1 \pm 0.3)\ \mu ms^{-1}$. In all three cases proportionality factors of order B = 1 – 10 k_BT are obtained and values for coarsening are smaller than for growth. While the conversion factors contain a large uncertainty, our data are qualitatively not incompatible with WF-like behaviour also for the case of ripening. A further qualitative check for the functional dependence is given in Fig. 18 where we plot the initial velocities normalised by their values at large Π^*_f. The bold line represents Eqn. (6), the thin dotted and solid lines represent a linear and square root dependence of v/v_∞ on Π^*_f, respectively. Our data support the idea of a WF-like dependence of initial ripening velocities on some suitably rescaled energy density, but clearly more accurate measurements are needed to quantitatively clarify this point.

Fig. 18: Normalised growth and initial ripening velocities versus the reduced energy density difference between melt and melt at freezing. The bold solid line is a fit of Eqn. (8) using $\Delta\mu = B\,\Pi^*_f$. The thin dotted and solid lines correspond to a linear and square root dependence of v/v_∞ on Π^*_f, respectively.

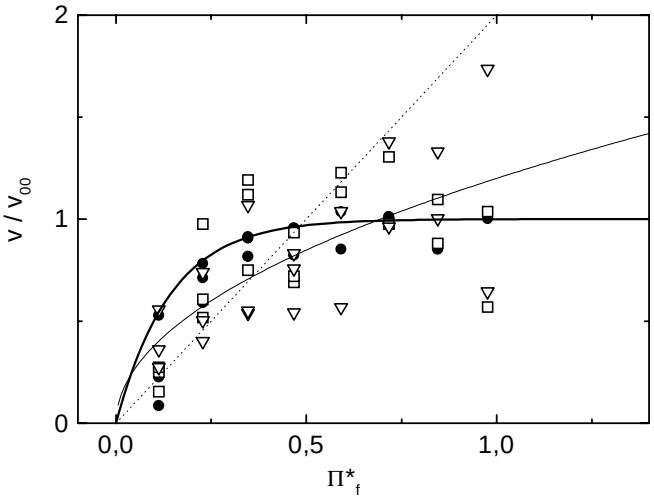

Discussion

We have given a detailed description of Bragg-microscopy including some representative examples of the kind of data accessible. We further compared the present set-up to other realisations of this principle. We found the technique to be extremely versatile and of great value to study the morphology or structure of colloidal solids including the corresponding temporal evolution. Also in future research this method combined from light scattering and microscopy has a large potential and should strengthen investigations of kinetic processes on the scale of several hundred particle distances.

We further presented measurements on the growth velocity of charged sphere crystals, there-

by again confirming the classical Wilson-Frenkel growth law for data taken above coexistence. We also observed specific deviations across coexistence and were able to discuss possible origins.
Finally we also investigated the ripening of columnar bcc twin domains. Here we found LAC-growth following a $t^{1/2}$ power law. The underlying reason for this is the decrease of defect density through the disappearance of twin boundaries at constant surface tension. Coarsening velocities are different for different crystallographic directions. Unexpectedly coarsening is aborted already during growth with only little dependence on the direction. A possible explanation was given in terms of a collective rearrangement involving an activated state. Further, for deionised samples coarsening velocities increased with increased particle number density. We thus obtained strong indications that a WF-law may also apply to initial coarsening velocities.

Acknowledgements
It is a pleasure to thank H. Löwen, P. Leiderer, J. Schwarz and R. Biehl for numerous intense discussions. We further are indepted to H.-J. Schöpe, J. Liu, M. Würth and S. von Hühnerbein for permission to reproduce their measurements and to I. Weber for providing micro-network sphere samples. Financial support of the DFG (SFB 306, SFB 262, Pa459/7-3, Pa459/8-1, Scha389/6-1,2), of the Materialwissenschaftliches Forschungszentrum Mainz (MWFZ) and of the HCM colloid physics network are gratefully acknowledged.

Bibliography
[1] **Robbins, M. O., Kremer, K., Grest, G. S.:** J. Chem. Phys. 1988, 88, 3286.
[2] **Voegtli, L. P., Zukoski IV, C. F.:** J. Colloid Interface Sci. 1991, 141, 79.
[3] **Bartlett, P., van Megen, W.:** In: Granular matter, An interdisciplinary approach; Mehta, A., Ed.; Springer: New York, 1994; p 195–257.
[4] **van Megen, W.:** Transp. Theory and Statist. Phys. 1995, 24, 1017.
[5] **Schöpe, H.-J., Decker, T., Palberg, T.:** J. Chem. Phys. 1998, 109, 10068.
[6] **Palberg, T.:** J. Phys. Condens. Matter 1999, 11, R323.
[7] **Ackerson, B. J.** (Ed): Phase Transitions 1990, 21.
[8] **Harland, J. L., van Megen, W.:** Phys. Rev. E 1996, 55, 3054.
[9] **Heymann, A., Stipp, A., Sinn, Chr., Palberg, T.:** J. Colloid Interface Sci. 1998, 206, 119.
[10] **He, Y., Ackerson, B. J., van Megen, W., Underwood, S. M., Schätzel, K.:** Phys. Rev. E 1996, 54, 5286.
[11] **Murray, C.:** MRS Bulletin 1998, 23, 33; van Blaaderen, A. ibid. 39.
[12] **Gast, A. P., Monovoukas, Y.:** Nature 1991, 351, 552.
[13] **Okubo, T.:** In: Macro-ion characterization: from dilute solution to complex fluids; Schmitz, K. S., Ed.; ACS Symposium Series, 1994, 548, 364.
[14] **Aastuen, D. J. W., Clark, N. A., Kotter, L. K., Ackerson, B. J.:** Phys. Rev. Lett. 1986, 57, 1733; Aastuen, D. J. W., Clark, N. A., Kotter, L. K., Ackerson, B. J.: Phys. Rev. Lett. 1986, 57, 2772 (Erratum).
[15] **Würth, M., Schwarz, J., Culis, F., Leiderer, P., Palberg, T.:** Phys. Rev. E 1995, 52, 6415.
[16] **Pieranski, P., Pansu, B.:** In: Atelier d'Hiver sur les Cristeaux colloideaux: Les Houches 1985; Pieranski, P., Rothen, F., Eds.; J. Phys. (France) C-3 1985, 46, 281.
[17] **Dhont, J. K. G.:** An introduction to the dynamics of colloids; Elsevier: Amsterdam, 1996.
[18] **G. Nägele:** Phys. Reports 1996 272, 217.
[19] **Liu, J., Schöpe, H.-J., Palberg, T.:** Part. Part. Syst. Charact.: 2000, 17, 206.
[20] **Dhont, J. K. G., Smits, C., Lekkerkerker, H. N. W. J.:** Colloid Interface Sci. 1992, 152, 386.
[21] **Palberg, T., Mönch, W., Schwarz, J., Leiderer, P.:** J. Chem. Phys. 1995, 102, 5082.
[22] **He, Y., Olivier, B., Ackerson, B. J.:** Langmuir 1997, 13, 1408.
[23] **Elliot, M. S., Bristol, B. T. F., Poon, W. C. K.:** Physica A 1997, 235, 216.
[24] **Loose, W., Ackerson, B. J.:** J. Chem. Phys. 1994, 101, 7211.

[25] **von Hünerbein, S., Würth, M., Palberg, T.:** Prog. Colloid & Polym. Sci 1996, 100, 241.
[26] **Maaroufi, M. R., Stipp, A., Palberg, T.:** Prog. Colloid & Polym. Sci 1998, 108, 83.
[27] **Evers, M., Garbow, N., Hessinger, D., Palberg, T.:** Phys. Rev. E 1998, 57, 6774.
[28] **Ackerson, B. J., Schätzel, K.:** Phys. Rev. E 1995, 52, 6448.
[29] **Russel, W. B., Chaikin, P. M., Zhu, J., Meyer, W. V., Rogers, R.:** Langmuir 1997, 13, 3871.
[30] **Stipp, A., Sinn, Chr., Palberg, T., Weber, I., Bartsch, E.:** Prog. Colloid & Polym. Sci 2000, 115, 59.
[31] **Dux, C., Versmold, H.:** Phys. Rev.Lett. 1997, 78, 1811.
[32] **Palberg, T.:** Curr. Opn. Colloid Interf. Sci. 1997, 2, 607.
[33] **Kelton, K. F.:** Solid State Physics 1993, 45, 75.

Corresponding author:
Prof. Dr. Thomas Palberg, Johannes Gutenberg-Universität Mainz, Institut für Physik, Staudingerweg 7, 55099 Mainz; e-mail: Thomas.Palberg@uni-mainz